FISEVIER

Contents lists available at ScienceDirect

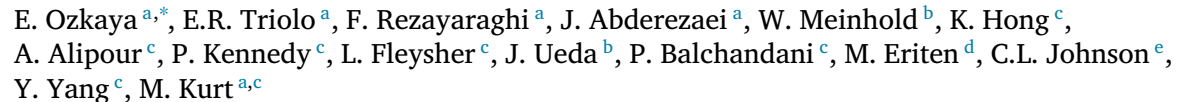
Journal of the Mechanical Behavior of Biomedical Materials

journal homepage: www.elsevier.com/locate/jmbbm



Research paper

Brain-mimicking phantom for biomechanical validation of motion sensitive MR imaging techniques



- ^a Department of Mechanical Engineering, Stevens Institute of Technology, Hoboken, NJ, 07030, USA
- b The George W. Woodruff of Mechanical Engineering, Georgia Institute of Technology, Atlanta, GA, 30332, USA
- ^c BioMedical Engineering and Imaging Institute, Icahn School of Medicine at Mount Sinai, New York, NY, 10029, USA
- d Department of Mechanical Engineering, University of Wisconsin-Madison, Madison, WI, 53706, USA
- ^e Department of Biomedical Engineering, University of Deleware, Newark, DE, 19716, USA

ARTICLE INFO

Keywords: Brain biomechanics Brain-mimicking phantom CINE imaging MR elastography

ABSTRACT

Motion sensitive MR imaging techniques allow for the non-invasive evaluation of biological tissues by using different excitation schemes, including physiological/intrinsic motions caused by cardiac pulsation or respiration, and vibrations caused by an external actuator. The mechanical biomarkers extracted through these imaging techniques have been shown to hold diagnostic value for various neurological disorders and conditions. Amplified MRI (aMRI), a cardiac gated imaging technique, can help track and quantify low frequency intrinsic motion of the brain. As for high frequency actuation, the mechanical response of brain tissue can be measured by applying external high frequency actuation in combination with a motion sensitive MR imaging sequence called Magnetic Resonance Elastography (MRE). Due to the frequency-dependent behavior of brain mechanics, there is a need to develop brain phantom models that can mimic the broadband mechanical response of the brain in order to validate motion-sensitive MR imaging techniques. Here, we have designed a novel phantom test setup that enables both the low and high frequency responses of a brain-mimicking phantom to be captured, allowing for both aMRI and MRE imaging techniques to be applied on the same phantom model. This setup combines two different vibration sources: a pneumatic actuator, for low frequency/intrinsic motion (1 Hz) for use in aMRI, and a piezoelectric actuator for high frequency actuation (30-60 Hz) for use in MRE. Our results show that in MRE experiments performed from 30 Hz through 60 Hz, propagating shear waves attenuate faster at higher driving frequencies, consistent with results in the literature. Furthermore, actuator coupling has a substantial effect on wave amplitude, with weaker coupling causing lower amplitude wave field images, specifically shown in the top-surface shear loading configuration. For intrinsic actuation, our results indicate that aMRI linearly amplifies motion up to at least an amplification factor of 9 for instances of both visible and sub-voxel motion, validated by varying power levels of pneumatic actuation (40%-80% power) under MR, and through video analysis outside the MRI scanner room. While this investigation used a homogeneous brain-mimicking phantom, our setup can be used to study the mechanics of non-homogeneous phantom configurations with bio-interfaces in the future.

1. Introduction

In the past two decades, mechanical characterization of soft tissues non-invasively has become increasingly widespread thanks to the emergence of Magnetic Resonance Elastography (MRE) (Muthupillai et al., 1995). In MRE, an external mechanical vibration source is driven in sync with the MRI machine by utilizing motion encoding gradients

(MEGs) (Hirsch et al., 2017; Tse et al., 2009). An inversion algorithm is then used to calculate stiffness maps (elastograms) of the material of interest using the resulting wave field information, captured at equally-spaced time offset points (Kolipaka et al., 2009; Papazoglou et al., 2008).

E-mail address: eozkaya@stevens.edu (E. Ozkaya).

^{*} Corresponding author.

MRE has been utilized as a diagnostic tool to measure the stiffness of the brain (Sack et al., 2009) to relate stiffness variations to diseases, such as multiple sclerosis (Wuerfel et al., 2010) and Alzheimer's disease (Murphy et al., 2011), to detect abnormalities such as meningioma brain tumors (Murphy et al., 2013; Chartrain et al., 2019), to capture pathological changes observed as in normal pressure hydrocephalus (Streitberger et al., 2011), or to study post-mortem changes in the brain tissue (Weickenmeier et al., 2018a). However, during MRE imaging of the brain, the cushioning caused by the skull, meninges, and cerebrospinal fluid (CSF) is a great stumbling block in capturing proper wave field images because these structures cause wave scattering and attenuation (Papazoglou et al., 2009). Recently, an alternative means of probing the mechanics of the brain has emerged with the realization of cardiac-induced physiological vibrations. The physiological vibrations inside the brain caused by cardiac-induced pulsatility features cerebral peduncle as the main vibration source, as opposed to the periphery of the skull as in the case of MRE. This motivated the possibility of elastography imaging at low frequency actuation to be investigated (Soellinger et al., 2009; Wagshul et al., 2011; Hirsch et al., 2013; Zorgani et al., 2015; Weaver et al., 2012; McGarry et al., 2015). Furthermore, it was realized that through phase-based video magnification, the motion caused by the physiological vibrations inside the brain can be detected without the need of an external vibration source, such as that used in MRE. In other words, lower harmonics, close to heartbeat frequency (~1 Hz), were able to be captured via amplified MRI (aMRI) by utilizing the aforementioned phase-based video magnification technique (Terem et al., 2018; Holdsworth et al., 2016; Abderezaei et al., 2021; Terem et al., 2021). This technique has the promise, for instance, to detect abnormal intracranial pressure and CSF flow related changes in conditions such as Chiari malformation I (Terem et al., 2018).

Recently, there has been an increasing interest in studying the low versus high frequency performance of MRE through phantom experiments (Gordon-Wylie et al., 2018; Solamen, 2019; Solamen et al., 2019; McGarry et al., 2019). This is needed since soft tissues are viscoelastic materials, and exhibit frequency-dependent mechanical behavior under harmonic loading. In this study, we mimic the cardiac-induced motion through inflating & deflating a flexible membrane and visualize this motion by performing aMRI. Furthermore, on the same phantom setup, we aim to investigate the effect of external vibration source positioning and its coupling with the tissue-mimicking phantom via MRE. The motivation in our study is to compare the aforementioned motion-sensitive MR imaging techniques, since they consider different frequency spectra for the biomechanical response of the brain tissue. Therefore, we designed a novel phantom test setup to enable both the low and high frequency actuation of the same brain-mimicking phantom to be captured via aMRI and MRE, respectively.

This is the first reported phantom study comparing aMRI and MRE across a range of frequencies to demonstrate the importance and value of combining these imaging methods. The combined knowledge of specific motion patterns in the brain under these two different frequency spectra can be useful for a variety of conditions, including brain tumors, Chiari Malformation I, and hydrocephalus by enabling a broadband mechanical characterization of the brain. For instance, the two important determinants for complete resection of brain tumors include degree of firmness/consistency and adhesiveness to the surrounding healthy brain tissue (Yin et al., 2017). With MRE, brain tumor consistency at fixed frequencies can be measured (Murphy et al., 2013; Hughes et al., 2015; Reiss-Zimmermann et al., 2015), while with aMRI, surface adhesion can potentially be quantified. In addition, for diseases such as hydrocephalus and Chiari malformation I, studying low and high frequency mechanical behavior of the brain through these two imaging modalities could be beneficial in identifying both the pathological and physiological changes that occur in these diseases (Buell et al., 2015; McAllister II, 2012).

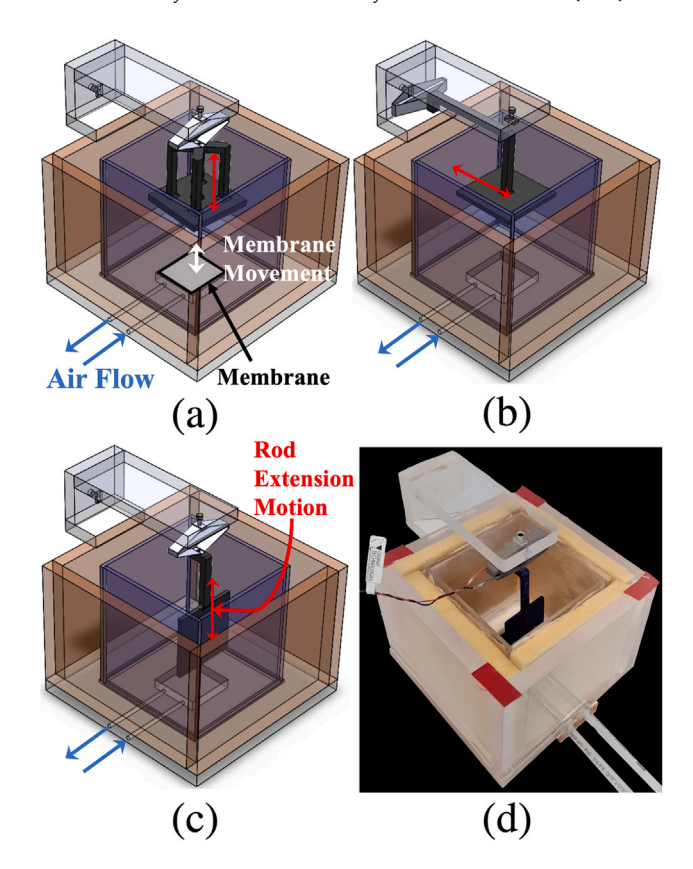


Fig. 1. Phantom test setup configuration with (a) rod extension causing harmonic loading through compression, (b) rod extension generating harmonic loading via shear force applied on the top surface, (c) rod extension creating harmonic loading along mid-plane via shear loading. (d) Manufactured test setup. The blue arrows indicate air flow for pneumatic driven motion during aMRI, and red arrows indicate rod extension motion direction during MRE.

2. Methods and materials

2.1. Phantom holder and actuator configurations

The phantom setup dimensions are chosen based on the MR head coil size in order to have a phantom with a volume similar to the human brain. A $15.20 \times 15.20 \text{ cm}^2$ square base piece with a $3.80 \times 3.80 \text{ cm}^2$ square cavity in the center (depth of 0.76 cm), and four outer side pieces (length 13.97 cm and height 10.16 cm), were cut from a 1.27 cm thick clear acrylic sheet (the orange components in Fig. 1(a-c)). The square cavity was covered with a flexible membrane to be used as the source of low frequency actuation when air is pumped into it. To allow air flow, one inlet and one outlet hole, each having a diameter of 0.30 cm with a distance of 1.90 cm in between, were drilled through one side of the base piece into the square cavity at the center (placement denoted by the blue "air flow" arrows in Fig. 1(a-c)). Plastic tubing was glued to the inlet and outlet holes to serve as air passages. Four pieces of 0.32 cm thick plexiglass sheet with a height of 10.41 cm and length of 9.84 cm were cut to be used as the inner walls of the setup (the purple components in Fig. 1(a-c)). These inner walls were then fixed in 0.25 cm deep slits on the base piece. For the positioning of the piezo actuator (APA150M, Cedrat Technologies), three pieces having a surface area of (length \times height) 5.08 \times 11.18 cm², 5.08 \times 5.08 cm², and 5.08×3.17 cm² were cut from 1.27 cm thick clear acrylic sheet and were attached to one of the outer walls as shown in Fig. 1 (the light gray/translucent components in Fig. 1(a-c)). The piezo actuator was attached to one of two positions, the first position shown in Fig. 1(a, c) and the second shown in Fig. 1(b). The spaces between inner and outer walls were filled with foam to isolate vibration transmission during

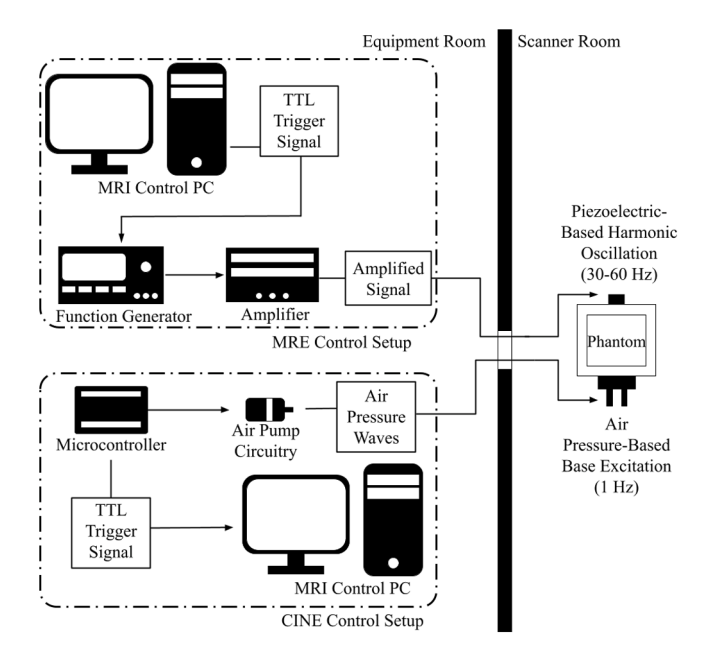


Fig. 2. Schematic of the MR phantom test setup with MRE control setup unit generating TTL trigger signal through the MRI control PC to drive a piezo electric actuator, and CINE control setup delivering TTL trigger signal from a microcontroller to trigger image acquisition. While the latter TTL signal is fed into the MRI scanner through a shielded BNC cable connection, the former is fed into the function generator through the external trigger input port. The MRE and CINE imaging are not performed simultaneously.

MRE imaging. Furthermore, the outer walls were fixed to the square base with double-sided tape to attenuate unwanted vibration delivery from the plexiglass sheets to the tissue-mimicking phantom. By taking these precautions, the 3D printed rod extensions attached to the piezo actuator as shown in three different configurations (Fig. 1(a-c)) became the only source of mechanical wave delivery. Each of the rod extensions had a 16.00 cm² flat square surface with a 0.32 cm thickness.

To inflate the flexible membrane, air was supplied to the phantom holder by two 12 V air pumps, each having a maximum operation pressure of 50 kPa. The air pumps were driven to inflate the flexible membrane at varying power levels, described here as the percentage of the maximum input voltage used to drive the pumps (e.g. 60% power is an input voltage of 60% of the maximum input voltage for the air pumps). Since CINE imaging is heartbeat-gated, in our setup, we needed to artificially replicate a heartbeat signal to establish gating between air pumping and CINE imaging period. A TTL pulse train of 5 V amplitude with a 50% duty cycle during 1 s, was sent to the MR scanner from the micro-controller (Fig. 2). For MRE imaging, the TTL trigger generated from the MRI control PC was fed into a function generator that controlled the driving frequency of the piezo actuator. The piezo actuator was able to generate maximum of 187 µm displacement during no-loading condition within the 0–200 Hz range.

Since gelatin type materials such as Knox, agar, and agarose are commonly used as a brain tissue surrogate for imaging method validation (Stewart et al., 2017), we chose Knox gelatin for phantom preparation. During each experiment, 49 ml Knox gelatin was dissolved in 700 ml water and then stirred for 2 min. The mixture was then heated in the microwave for 80 s. Afterwards, the mixture was poured into the phantom holder, using a mesh strainer to remove any small residues. This was followed by degassing the phantom test setup to remove any air bubbles trapped inside the gelatin phantom medium.

2.2. Imaging protocol

While performing MRE imaging, the MRE sequence provided TTL triggering to drive the piezo actuator in sync with the motion encoding

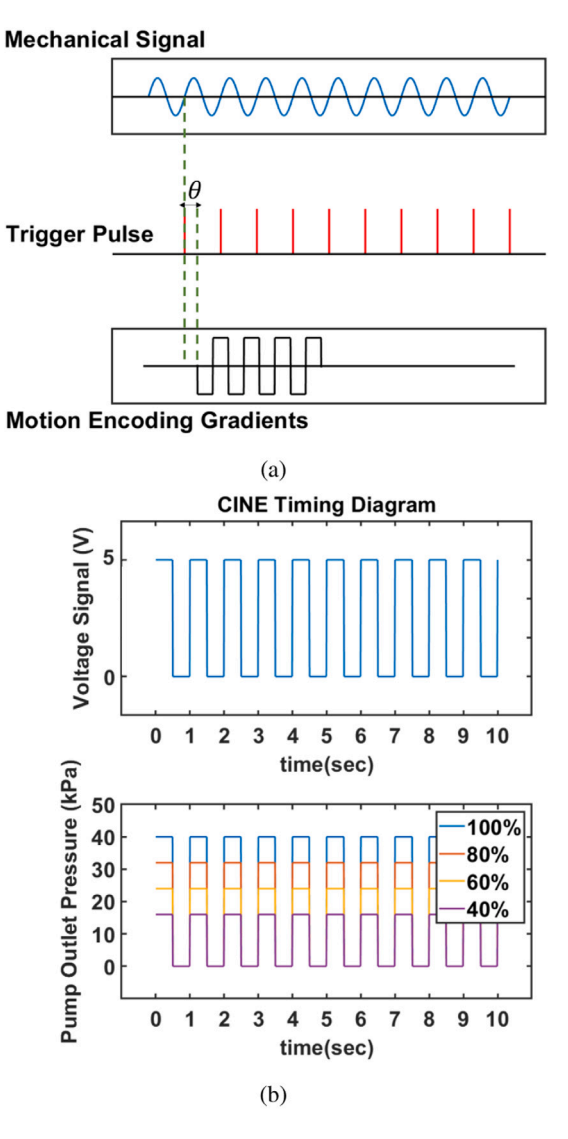


Fig. 3. Timing diagram of the imaging sequences for (a) MRE and (b) CINE scans. θ is the phase offset between the trigger pulse train and the Motion Encoding Gradients. Legends shown in CINE timing diagram are the air pump power levels.

gradients (Fig. 3(a)). MRE data was then acquired for 24 slices with 3D motion encoding gradients using an echo planar spin echo 2D pulse sequence (Chaze et al., 2019) in the coronal and axial planes with the following imaging parameters: acquisition matrix = 96×96 , flip angle = 90, FOV = 240 mm, 8 phase offsets, slice thickness = 2.5 mm, gradient amplitude = 40 mT/m, mechanical vibration frequencies of 30 to 60 Hz (5 Hz increment), and additional frequency-dependent imaging parameters for MRE imaging, such as the Echo Time (TE) and Repetition Time (TR), are listed in Table 1. The fixed-free maximum mechanical vibration amplitude is 187 µm, and we estimate the loaded amplitude to be approximately 100 µm in 30-60 Hz cases. For CINE imaging, the TTL triggering was provided to the scanner through the microcontroller while the air pump was driven with the same duty cycle as the TTL triggering signal (Fig. 3(b)). Five different power levels ranging from 30% to 80% (in 10% increments) were used during CINE imaging. In other words, outlet pressure of the air pumps connected in series is varied from 15 kPa up to 40 kPa in 5 kPa increments. The parameters for CINE imaging were as follows: TE = 1.3 ms, TR = 3.3 ms, flip angle = 42, acquisition matrix = 256×256 , and 88 synthetic cardiac phases per-RR interval, resulting in a 10 ms temporal resolution. All the experiments are performed inside of a 3-Tesla Siemens Skyra

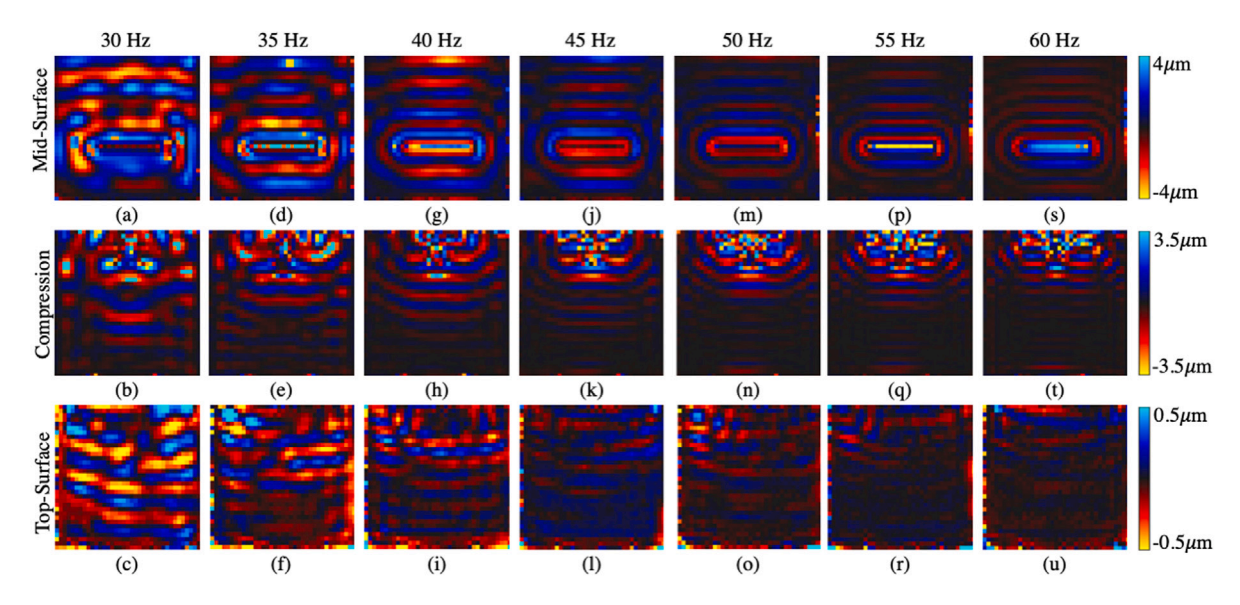


Fig. 4. Displacement fields captured during MRE imaging for (a-c) 30 Hz, (d-f) 35 Hz, (g-i) 40 Hz, (j-l) 45 Hz, (m-o) 50 Hz, (p-r) 55 Hz, and (s-u) 60 Hz driving frequencies. First row shows shear waves propagating under mid-surface shear loading parallel to the base while second and third rows depict the shear waves propagating during compression and top-surface shear loading respectively parallel to the front surface.

Table 1 MRE Scanning Parameters.

Frequency (Hz)	TR (ms)	TE (ms)
30	4803.8	113.0
35	4124.2	101.0
40	3605.8	92.0
45	3736.3	85.0
50	3840.0	80.0
55	3502.1	75.0
60	3210.2	71.0

scanner with a 32-channel head coil (Siemens Healthineers; Erlangen, Germany).

2.3. Displacement fields acquired via mre and amri

To acquire the displacement fields from MRE and aMRI experiments, two different methods were implemented. Spatial mapping of displacement patterns under external harmonic loading is performed using MRE, which is a phase-contrast MRI technique. In MRE, induced phase shift in the NMR signal due to external mechanical loading at location *r* at a given frequency within a medium is given by Eq. (1) (Manduca et al., 2001).

$$\phi(\vec{r},\theta) = \frac{2\gamma NT(\overrightarrow{G_0} \cdot \overrightarrow{\zeta_0})}{\pi} \cos(\vec{k} \cdot \vec{r} + \theta)$$
 (1)

 \vec{r} is the position vector, γ is the gyromagnetic ratio, N is the gradient pairs, T is the period of the motion encoding gradient (MEG), $\overline{G_0}$ is the amplitude of MEG, \vec{k} is the wave number, and ζ_0 is the peak amplitude of motion. MEGs convolve over the cyclic motion components of the location r along each orthogonal direction. θ , which is the phase offset between the MEGs and the external mechanical loading, is varied gradually throughout the whole period of the cyclic motion. This allows propagating wave fields to be captured at different time points within a single cyclic motion period.

For aMRI, a video of the unamplified motion is created through the captured CINE images to observe the motion caused by cyclic pressure loading. Later, the video was amplified using an octave pyramid shaped phase-based amplification algorithm with a sampling rate of 88 Hz due to 88 time captures per scan with a bandpass filter having a lower cutoff frequency of 0.5 Hz and a higher cutoff frequency of 2 Hz, and

an amplification factor of either 1, 3, 5, 6, 7, or 9. To acquire the displacement maps of the aMRI results, a non-parametric diffeomorphic image registration based on the Thirion's Demons algorithm was implemented (Vercauteren et al., 2007). Here, the first snapshot from aMRI, referred to as the reference image frame, was used as a fixed image and the images at other time points were referred to as moving images. The Demons algorithm performed an optimization procedure between the fixed and moving images, in order to find the optimal displacement of each pixel such that the moving images were aligned with respect to the reference image (Vercauteren et al., 2007). The Demons algorithm used the gradient information from the fixed image to determine the force of the demons needed to warp the moving image (Wang et al., 2005; Cachier et al., 2003; Haber and Modersitzki, 2004). Therefore, the standard deviation for each pixel in the image compared to the first frame of the video was calculated. Terem et al. (2018). Furthermore, with a linear potentiometer that has a maximum stroke of 11 mm, the displacement of the membrane under 40%, 60%, 80%, and 100% air pump power levels were recorded as 4.24, 4.75, 4.86, and 5.25 mm respectively.

3. Results

3.1. Displacement fields acquired via mre

During MRE imaging, wave propagation fields were captured under mid-surface shear, top-surface shear and compression loading. The Gaussian filtered (σ =2) shear wave fields for the mid-surface loading configuration were visualized in the 4th phase offset and 45.0 mm from the top of the phantom surface. Similarly, the Gaussian filtered (σ =2) shear wave fields for the compression loading configuration were visualized in the 1st phase offset and 41.9 mm from the front the phantom, and in its 4th phase offset and 18.3 mm from the front of the phantom for the top-surface loading configuration.

For the mid-surface, compression, and top-surface loading conditions, the absolute maximum amplitudes were 4.0 $\mu m,~3.6~\mu m,$ and 0.55 $\mu m,$ respectively. These maximum amplitudes were used to set the scales for the visualization of the shear waves for each loading configuration (Fig. 4). The amplitudes of the shear wave produced by the top surface shear loading were lower than those produced by the other two loading conditions, indicating weaker coupling between the phantom surface and the actuator than the other two configurations.

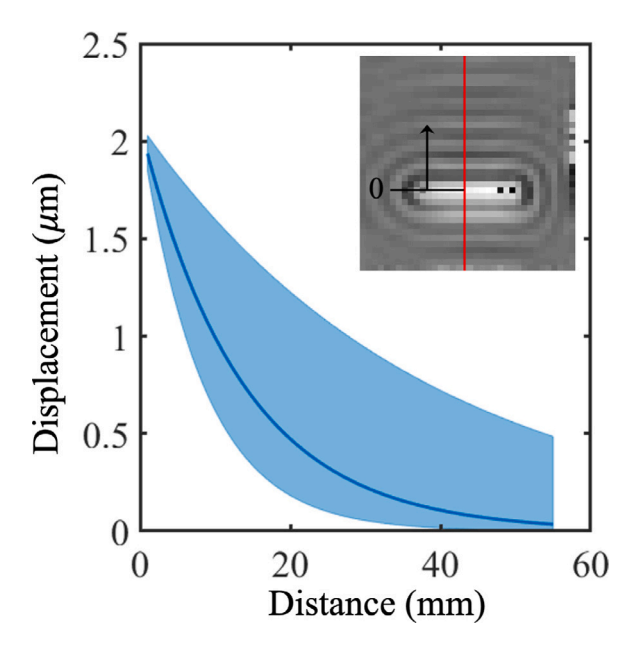


Fig. 5. Acquired exponential decay rate for phase offsets 4 through 8 under midsurface shear loading at 60 Hz driving frequency. The image in the upper right shows the 2D wave field data of the 4th phase offset where the red line indicates where data points were acquired for the 1D wave profile. The line plot shows the average exponential decay rate for the cropped 1D wave profile for phase offsets 4 through 8 using the fit function $A.e^{-\alpha x}$. The blue line is the average decay profile and the shaded area indicates standard deviation.

By using the fit function $A.e^{-\alpha x}$ for the wave field data collected along the red line at 8 different phase offsets (see Fig. 5), mean and standard deviation of the exponential decay rate is acquired (Yin et al., 2008). This procedure is performed only for the mid-surface shear loading configuration because of the coupling between the brain-mimicking phantom and the 3D printed rod extension tip being stronger than the other two. For 30 Hz harmonic loading, while the average decay rate for phase offsets 4 through 8 was $11.4 \pm 4.1 \text{ m}^{-1}$ for 60 Hz harmonic loading it increased to $74.1 \pm 47.6 \text{ m}^{-1}$.

3.2. Displacement fields acquired via amri

The results of the previously described phase-based amplification and subsequent non-parametric diffeomorphic image registration analysis are visualized as both a video and a snapshot (Vid. 1, supplementary material), at the time point with maximum deformation of the base membrane (Fig. 6) to detect harmonic displacements. As the amplification factor increased, so did the magnitude of the motion in the image, specifically near the bottom of the image close to the source of the actuation caused by the flexible membrane motion. At the 80% power level, there was a 64.8% increase in the absolute maximum displacement amplitude over time when amplifying by a factor of 6. At the 60% and 40% power levels, these absolute maximums increased by 83% and 94%, respectively. These absolute maximum values are all found near the bottom of the phantom, close to the actuating membrane. By looking at the plot of the absolute maximum displacement over all time points for each pixel in the slice, the motion caused by the base membrane travels farther up the phantom at higher power levels, indicating larger wave propagation as base membrane moves with greater air pressure, also visualized in the aMRI maximum membrane amplitude time slices (Fig. 6). These displacement fields qualitatively approximate the displacement patterns observed in the piston-like intrinsic motion of the human brain (Terem et al., 2018)

However, it is observed that there is a lower limit of motion that can be captured for amplification to generate a displacement map with a motion signal higher than the noise itself (Fig. 6). Motion analysis

at 30% power levels were omitted due to a lack of amplification of significant base membrane motion. The motion analysis at 40% power shows minimal amplified base membrane motion, but amplification of movement by the membrane is still observed due to motion by the left portion of the base membrane (Fig. 6(g-i)). This distinction between noise and base membrane motion is also supported by the previously mentioned plots of maximum displacement over all time points, where the maximum displacement values are concentrated at the left side of the phantom at 40% power, but there is no such concentration of maximum displacement values near the base membrane at 30% power.

To evaluate the linearity of the amplification process for the MRI measurements used in this investigation, the absolute maximum displacement value for representative power levels of 40%, 60%, and 80% at amplification factors of 1, 3, 5, 7, and 9 were calculated (Fig. 7) and a linear regression analysis was performed per power level. The resulting R-squared values (40%: 0.96, 60%: 0.98, 80%: 0.95) indicate a strong positive linear correlation between absolute maximum displacement and amplification factor for all representative power levels. These results indicate that our brain-mimicking phantom could be used for up to an amplification factor of 9 at the tested actuation levels without introducing artifacts.

To verify the displacement performance of the system and the linearity of the amplification process for the amplification factors used in this investigation, the phantom test setup was rotated 90 degrees from its shown configuration in Fig. 1 and was filled half-way with the same Knox gelatin mixture described previously such that half the membrane was covered. A temporary "tattoo" grid of 0.5 cm x 0.5 cm was drawn onto the surface of the phantom perpendicular to the membrane, and a slow motion video (240 frames per second) was taken of the membrane and phantom movement at representative power levels of 40%, 60%, and 80%. These videos were then masked to the location of the red rectangle (region of interest) shown on the top left phantom image of Fig. 6 amplified using representative amplification levels of 0, 3, and 6 as shown on the right portion of Fig. 6. These amplified videos (Vid. 2, supplementary material) were manually motion-tracked in ImageJ using three cross-hair locations closest to the membrane on the phantom's grid pattern to determine the maximum amplitude at each characteristic power level and amplification factor. A linear regression analysis was then performed at each power level to compare real-life measurements to those captured under MR, as well as to verify the linearity of amplifying real-life slow-motion video (Fig. 7). The resulting R-squared values (40%: 0.99, 60%: 0.99, 80%: 0.98) indicate a strong positive linear correlation between absolute maximum displacement and amplification factor for all representative power levels in slow motion video as well, matching our MRI results. Performing three paired t-tests (one for each of the power-level matched data sets), no significant differences were found between displacement measurements performed under MRI and displacement measurements performed on slow-motion video (p > 0.40). This lack of difference in displacement measurements over multiple amplification factors and across the representative power levels can also be seen in Fig. 7. These displacement measurements combined with linear potentiometer measurements of the membrane motion, however, do indicate that air-pump output is not linear proportional to voltage input, which was the metric used to determine "percentage power level".

4. Discussion

In the past decade, significant interest has been shown in understanding the mechanical properties of the brain tissue (Miller et al., 2000; Finan et al., 2017; Shafiee et al., 2016). With MRE being known as virtual palpation, it became possible to obtain the mechanical properties of brain tissue in a non-invasive manner (Hiscox et al., 2016; Xu et al., 2007; Braun et al., 2014; Weickenmeier et al., 2018b; Kruse et al., 2008; Sack et al., 2009; Lv et al., 2020). However, the brain being encased inside the skull presents challenges during imaging, specifically

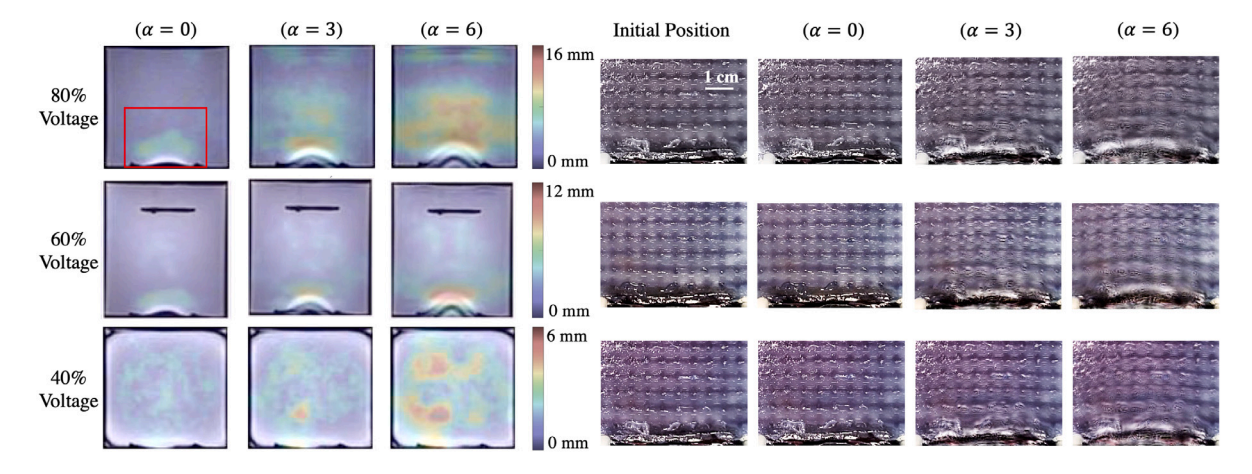


Fig. 6. Amplified MRI (aMRI) displacement plots, shown in units of millimeters, captured at the time point with maximum deformation for vertical mid-slice during 80% air pump voltage, 60% voltage, and 40% voltage with amplification factors of 6, 3, and 0 (as labeled). This was captured both using MRI (left) and using slow motion video for validation (right). The red box in the upper left MRI-based displacement image indicates the region of interest, which is also the area in which the slow motion video frames are extracted for analysis.

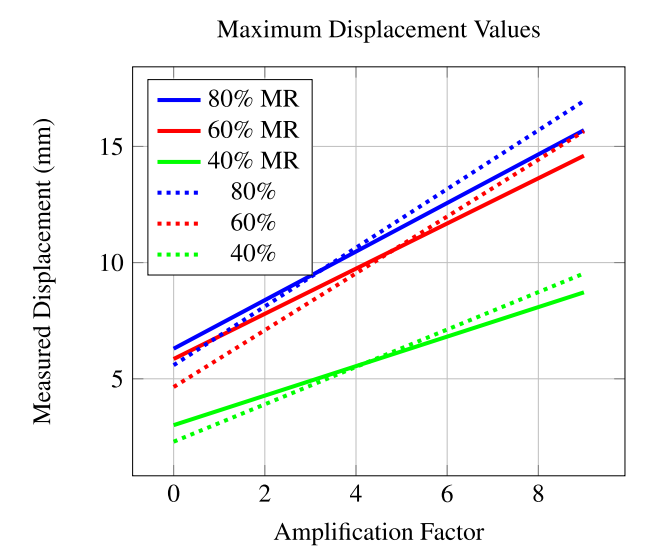


Fig. 7. Linear regression showing amplification factor versus absolute maximum displacement amplitude trend for MRI and video measurements for 40% (green solid), 60% (red solid), and 80% (blue solid) air pump power levels (percentage of maximum voltage applied to air pumps) in MR acquisition and for 40% (green dotted), 60% (red dotted), and 80% (blue dotted) air pump power levels in slow-motion video acquisition. R-squared values for linear regressions are 0.96, 0.98, 0.95, 0.99, and 0.98 respectively. No significant differences were found between 80% MR and 80% video, 60% MR and 60% video, or 40% MR and 40% video displacement measurements using paired t-tests (p > 0.4).

while imaging the deep white matter regions of the brain (Clayton et al., 2012).

As a complementary technique, the motion caused by cardiac-induced movement at the brainstem can be utilized as an intrinsic vibration source during each heartbeat without the need for an external mechanical driver (Holdsworth et al., 2016; Terem et al., 2018; Abderezaei et al., 2020). With this study, through MRI and slow-motion video experiments on a novel phantom test setup, we showed that both of these non-invasive *in vivo* mechanical imaging techniques can be complementary and merged to enhance the understanding of human brain biomechanics. Furthermore, we evaluated the performance of both these techniques on a homogeneous brain-mimicking phantom and determined the feasibility limits of the imaging sequences in terms of capturing the induced wave fields.

As anticipated, during MRE imaging under higher frequency loading, more wave attenuation is observed than at lower frequency loading (Fig. 4). Furthermore, differences in mechanical driver surface coupling with the tissue-mimicking phantom caused changes in the amplitude of the displacement fields captured. For mid-surface shear loading, because the 3D printed rod extension was dipped inside the phantom volume, the delivery of the shear waves were more apparent. In addition, for the mid-surface shear and compression loading scenarios, the maximum displacement amplitude was higher then the top surface shear loading configuration. We suspect that this might be due to the extra resistive force caused by the weight of the L-shaped rod extension tip, or weaker coupling between the actuation surface and the phantom. In the other two configurations, the dead weight of the rod extensions were not impeding the generated motion by the piezo-actuator. Finally, the ability to determine which portion of the base membrane moves the most due to amplification via aMRI means that this technique can likely be used to determine the low-frequency movement properties of specific regions of the brain. By knowing the strengths and shortcomings of both these mechanical imaging techniques, a more comprehensive diagnosis can be performed using the low and high frequency response of the human brain under harmonic loading.

Our phantom setup paves the way for the understanding of broadband brain biomechanics by enabling different actuation modalities simultaneously. As a viscoelastic biomaterial with intricate geometrical details, the mechanics of the human brain has been used in different clinical conditions to aid diagnosis, prognosis and interventions. The combined framework of aMRI and MRE together can be used in cases where there are prominent changes in both the physiological flow dynamics and pathology of the brain, such as in brain tumors (Murphy et al., 2013; Hughes et al., 2015), Chiari I Malformation (Holdsworth et al., 2016; Terem et al., 2018), and abnormalities in the brain arteries (Abderezaei et al., 2020). In addition, both techniques could aid the diagnosis of the stage of hydrocephalus without damaging the bony cranium by using a cerebral shunt. Since tissue-mimicking phantoms provide full control on the material properties and geometry, more complex phantoms can be created to incorporate the other complex elements in the brain. For instance, the efficacy of both imaging techniques can further be investigated by preparing phantoms having tumor like inclusions with varying stiffness values (Gordon-Wylie et al., 2018; McGarry et al., 2019; Solamen, 2019; Solamen et al., 2019).

5. Conclusion

In this work, we developed a novel tissue-mimicking phantom test setup that can be used with both aMRI and MRE imaging methods. During aMRI, air pump power levels were varied while in MRE, external harmonic loading frequency and mechanical loading source configuration were varied to capture a wide range of displacement amplitudes and characteristics. For different loading conditions in MRE, we observed a substantial change in the measured displacement fields, with the mid-surface loading condition producing the highest signal-to-noise ratio and displacement amplitudes. Concurrently, we determined the feasibility limits of our amplification algorithm for aMRI at different air pump actuation levels and found that the relationship between the amplification levels and measured displacements stay linear up to an amplification factor of 9, which was also validated through slow-motion video experiments outside the MRI scanner room. Our brain-mimicking phantom setup paves the way for a broadband characterization and validation of the human brain biomechanics by enabling different actuation modalities simultaneously.

CRediT authorship contribution statement

E. Ozkaya: Conceptualization, Data curation, Formal analysis, Investigation, Methodology, Visualization, Writing - review & editing. E.R. Triolo: Data curation, Formal analysis, Investigation, Visualization, Writing - review & editing. F. Rezayaraghi: Visualization, Formal analysis, Writing - review & editing. J. Abderezaei: Visualization, Formal analysis, Writing - review & editing. W. Meinhold: Methodology, Writing - review & editing. K. Hong: Investigation, Resources, Software, Validation. A. Alipour: Resources, Software, Writing - review & editing. P. Kennedy: Investigation, Resources, Software, Validation. L. Fleysher: Investigation, Resources, Software, Validation. J. Ueda: Resources. P. Balchandani: Resources, Software, Writing - review & editing. M. Eriten: Conceptualization, Funding acquisition, Supervision, Writing - review & editing. C.L. Johnson: Software, Writing - review & editing. Y. Yang: Resources, Software. M. Kurt: Project administration, Conceptualization, Funding acquisition, Resources, Supervision, Writing - review & editing.

Acknowledgments

We acknowledge Kamil Banibaker and Dewey Chu for their support during the experiments. This study was funded by NSF, United States award 1826270.

Appendix A. Supplementary data

Supplementary material related to this article can be found online at https://doi.org/10.1016/j.jmbbm.2021.104680.

References

- Abderezaei, J., Martinez, J., Terem, I., Fabris, G., Pionteck, A., Yang, Y., Holdsworth, S.J., Nael, K., Kurt, M., 2020. Amplified Flow Imaging (aFlow): A novel MRI-based tool to unravel the coupled dynamics between the human brain and cerebrovasculature. IEEE Trans. Med. Imaging.
- Abderezaei, J., Pionteck, A., Terem, I., Dang, L., Scadeng, M., Morgenstern, P., Shrivastava, R., Holdsworth, S.J., Yang, Y., Kurt, M., 2021. Development, calibration, and testing of 3D amplified MRI (aMRI) for the quantification of intrinsic brain motion. Brain Multiphys. 100022.
- Braun, J., Guo, J., Lützkendorf, R., Stadler, J., Papazoglou, S., Hirsch, S., Sack, I., Bernarding, J., 2014. High-resolution mechanical imaging of the human brain by three-dimensional multifrequency magnetic resonance elastography at 7T. Neuroimage 90, 308–314.
- Buell, T.J., Heiss, J.D., Oldfield, E.H., 2015. Pathogenesis and cerebrospinal fluid hydrodynamics of the Chiari I malformation. Neurosurg. Clin. N. Am. 26 (4), 495.
- Cachier, P., Bardinet, E., Dormont, D., Pennec, X., Ayache, N., 2003. Iconic feature based nonrigid registration: the PASHA algorithm. Comput. Vis. Image Underst. 89 (2–3), 272–298.
- Chartrain, A.G., Kurt, M., Yao, A., Feng, R., Nael, K., Mocco, J., Bederson, J.B., Balchandani, P., Shrivastava, R.K., 2019. Utility of preoperative meningioma consistency measurement with magnetic resonance elastography (MRE): a review. Neurosurg. Rev. 42 (1), 1–7.

- Chaze, C.A., McIlvain, G., Smith, D.R., Villermaux, G.M., Delgorio, P.L., Wright, H.G., Rogers, K.J., Miller, F., Crenshaw, J.R., Johnson, C.L., 2019. Altered brain tissue viscoelasticity in pediatric cerebral palsy measured by magnetic resonance elastography. NeuroImage: Clin. 22, 101750.
- Clayton, E.H., Genin, G.M., Bayly, P.V., 2012. Transmission, attenuation and reflection of shear waves in the human brain. J. R. Soc. Interface 9 (76), 2899–2910.
- Finan, J.D., Sundaresh, S.N., Elkin, B.S., McKhann II, G.M., Morrison III, B., 2017. Regional mechanical properties of human brain tissue for computational models of traumatic brain injury. Acta Biomater. 55, 333–339.
- Gordon-Wylie, S.W., Solamen, L.M., McGarry, M.D., Zeng, W., VanHouten, E., Gilbert, G., Weaver, J.B., Paulsen, K.D., 2018. MR Elastography at 1 Hz of gelatin phantoms using 3D or 4D acquisition. J. Magn. Reson. 296, 112–120.
- Haber, E., Modersitzki, J., 2004. Numerical methods for volume preserving image registration. Inverse Problems 20 (5), 1621.
- Hirsch, S., Braun, J., Sack, I., 2017. Magnetic Resonance Elastography: Physical Background and Medical Applications. John Wiley & Sons.
- Hirsch, S., Klatt, D., Freimann, F., Scheel, M., Braun, J., Sack, I., 2013. In vivo measurement of volumetric strain in the human brain induced by arterial pulsation and harmonic waves. Magn. Reson. Med. 70 (3), 671–683.
- Hiscox, L.V., Johnson, C.L., Barnhill, E., McGarry, M.D., Huston 3rd, J., Van Beek, E.J., Starr, J.M., Roberts, N., 2016. Magnetic resonance elastography (MRE) of the human brain: technique, findings and clinical applications. Phys. Med. Biol. 61 (24) R401
- Holdsworth, S.J., Rahimi, M.S., Ni, W.W., Zaharchuk, G., Moseley, M.E., 2016.
 Amplified magnetic resonance imaging (aMRI). Magn. Reson. Med. 75 (6), 2245–2254.
- Hughes, J.D., Fattahi, N., Van Gompel, J., Arani, A., Meyer, F., Lanzino, G., Link, M.J., Ehman, R., Huston, J., 2015. Higher-resolution magnetic resonance elastography in meningiomas to determine intratumoral consistency. Neurosurgery 77 (4), 653–659.
- Kolipaka, A., McGee, K.P., Manduca, A., Romano, A.J., Glaser, K.J., Araoz, P.A., Ehman, R.L., 2009. Magnetic resonance elastography: Inversions in bounded media. Magn. Reson. Med. 62 (6), 1533–1542.
- Kruse, S.A., Rose, G.H., Glaser, K.J., Manduca, A., Felmlee, J.P., Jack, Jr., C.R., Ehman, R.L., 2008. Magnetic resonance elastography of the brain. Neuroimage 39 (1), 231–237.
- Lv, H., Kurt, M., Zeng, N., Ozkaya, E., Marcuz, F., Wu, L., Laksari, K., Camarillo, D.B., Pauly, K.B., Wang, Z., et al., 2020. MR elastography frequency-dependent and independent parameters demonstrate accelerated decrease of brain stiffness in elder subjects. Eur. Radiol. 1–10.
- Manduca, A., Oliphant, T.E., Dresner, M.A., Mahowald, J., Kruse, S.A., Amromin, E., Felmlee, J.P., Greenleaf, J.F., Ehman, R.L., 2001. Magnetic resonance elastography: non-invasive mapping of tissue elasticity. Med. Image Anal. 5 (4), 237–254.
- McAllister II, J.P., 2012. Pathophysiology of congenital and neonatal hydrocephalus. In: Seminars in Fetal and Neonatal Medicine, Vol. 17, No. 5. Elsevier, pp. 285–294.
- McGarry, M., Johnson, C., Sutton, B., Georgiadis, J., Van Houten, E., Pattison, A., Weaver, J., Paulsen, K., 2015. Suitability of poroelastic and viscoelastic mechanical models for high and low frequency MR elastography. Med. Phys. 42 (2), 947–957.
- McGarry, M., Van Houten, E., Solamen, L., Gordon-Wylie, S., Weaver, J., Paulsen, K., 2019. Uniqueness of poroelastic and viscoelastic nonlinear inversion MR elastography at low frequencies. Phys. Med. Biol. 64 (7), 075006.
- Miller, K., Chinzei, K., Orssengo, G., Bednarz, P., 2000. Mechanical properties of brain tissue in-vivo: experiment and computer simulation. J. Biomech. 33 (11), 1369–1376.
- Murphy, M.C., Huston, J., Glaser, K.J., Manduca, A., Meyer, F.B., Lanzino, G., Morris, J.M., Felmlee, J.P., Ehman, R.L., 2013. Preoperative assessment of meningioma stiffness using magnetic resonance elastography. J. Neurosur. 118 (3), 643–648.
- Murphy, M.C., Huston III, J., Jack, Jr., C.R., Glaser, K.J., Manduca, A., Felmlee, J.P., Ehman, R.L., 2011. Decreased brain stiffness in Alzheimer's disease determined by magnetic resonance elastography. J. Magn. Reson. Imaging 34 (3), 494–498.
- Muthupillai, R., Lomas, D., Rossman, P., Greenleaf, J.F., Manduca, A., Ehman, R.L., 1995. Magnetic resonance elastography by direct visualization of propagating acoustic strain waves. Science 269 (5232), 1854–1857.
- Papazoglou, S., Hamhaber, U., Braun, J., Sack, I., 2008. Algebraic Helmholtz inversion in planar magnetic resonance elastography. Phys. Med. Biol. 53 (12), 3147.
- Papazoglou, S., Xu, C., Hamhaber, U., Siebert, E., Bohner, G., Klingebiel, R., Braun, J., Sack, I., 2009. Scatter-based magnetic resonance elastography. Phys. Med. Biol. 54 (7) 2229
- Reiss-Zimmermann, M., Streitberger, K.-J., Sack, I., Braun, J., Arlt, F., Fritzsch, D., Hoffmann, K.-T., 2015. High resolution imaging of viscoelastic properties of intracranial tumours by multi-frequency magnetic resonance elastography. Clin. Neuroradiol. 25 (4), 371–378.
- Sack, I., Beierbach, B., Wuerfel, J., Klatt, D., Hamhaber, U., Papazoglou, S., Martus, P., Braun, J., 2009. The impact of aging and gender on brain viscoelasticity. Neuroimage 46 (3), 652–657.
- Shafiee, A., Ahmadian, M.T., Hoviattalab, M., 2016. Mechanical characterization of brain tissue in compression. In: International Design Engineering Technical Conferences and Computers and Information in Engineering Conference, Vol. 50138. American Society of Mechanical Engineers, V003T11A001.
- Soellinger, M., Rutz, A.K., Kozerke, S., Boesiger, P., 2009. 3D cine displacement-encoded MRI of pulsatile brain motion. Magn. Reson. Med. 61 (1), 153–162.

- Solamen, L.M., 2019. Advancements in Magnetic Resonance Poroelastography Using Intrinsic Activation (Ph.D. dissertation). Dartmouth College.
- Solamen, L.M., Gordon-Wylie, S.W., McGarry, M.D., Weaver, J.B., Paulsen, K.D., 2019. Phantom evaluations of low frequency MR elastography. Phys. Med. Biol. 64 (6), 065010.
- Stewart, D.C., Rubiano, A., Dyson, K., Simmons, C.S., 2017. Mechanical characterization of human brain tumors from patients and comparison to potential surgical phantoms. PLoS One 12 (6), e0177561.
- Streitberger, K.-J., Wiener, E., Hoffmann, J., Freimann, F.B., Klatt, D., Braun, J., Lin, K., McLaughlin, J., Sprung, C., Klingebiel, R., et al., 2011. In vivo viscoelastic properties of the brain in normal pressure hydrocephalus. NMR Biomed. 24 (4), 385–392.
- Terem, I., Dang, L., Champagne, A., Abderezaei, J., Pionteck, A., Almadan, Z., Lydon, A.-M., Kurt, M., Scadeng, M., Holdsworth, S.J., 2021. 3D amplified MRI (aMRI). Magn. Reson. Med. 86 (3), 1674–1686.
- Terem, I., Ni, W.W., Goubran, M., Rahimi, M.S., Zaharchuk, G., Yeom, K.W., Moseley, M.E., Kurt, M., Holdsworth, S.J., 2018. Revealing sub-voxel motions of brain tissue using phase-based amplified MRI (aMRI). Magn. Reson. Med. 80 (6), 2549–2559.
- Tse, Z., Janssen, H., Hamed, A., Ristic, M., Young, I., Lamperth, M., 2009. Magnetic resonance elastography hardware design: a survey. Proc. Inst. Mech. Eng. H 223 (4), 497–514.
- Vercauteren, T., Pennec, X., Perchant, A., Ayache, N., 2007. Non-parametric diffeomorphic image registration with the demons algorithm. In: International Conference on Medical Image Computing and Computer-Assisted Intervention. Springer, pp. 319–326.
- Wagshul, M.E., Eide, P.K., Madsen, J.R., 2011. The pulsating brain: a review of experimental and clinical studies of intracranial pulsatility. Fluids Barriers CNS 8 (1), 1–23.

- Wang, H., Dong, L., O'Daniel, J., Mohan, R., Garden, A.S., Ang, K.K., Kuban, D.A., Bonnen, M., Chang, J.Y., Cheung, R., 2005. Validation of an accelerated 'demons' algorithm for deformable image registration in radiation therapy. Phys. Med. Biol. 50 (12), 2887.
- Weaver, J.B., Pattison, A.J., McGarry, M.D., Perreard, I.M., Swienckowski, J.G., Eskey, C.J., Lollis, S.S., Paulsen, K.D., 2012. Brain mechanical property measurement using MRE with intrinsic activation. Phys. Med. Biol. 57 (22), 7275.
- Weickenmeier, J., Kurt, M., Ozkaya, E., de Rooij, R., Ovaert, T., Ehman, R.L., Pauly, K.B., Kuhl, E., 2018a. Brain stiffens post mortem. J. Mech. Behav. Biomed. Mater. 84, 88–98.
- Weickenmeier, J., Kurt, M., Ozkaya, E., Wintermark, M., Pauly, K.B., Kuhl, E., 2018b.
 Magnetic resonance elastography of the brain: a comparison between pigs and humans. J. Mech. Behav. Biomed. Mater. 77, 702–710.
- Wuerfel, J., Paul, F., Beierbach, B., Hamhaber, U., Klatt, D., Papazoglou, S., Zipp, F., Martus, P., Braun, J., Sack, I., 2010. MR-elastography reveals degradation of tissue integrity in multiple sclerosis. Neuroimage 49 (3), 2520–2525.
- Xu, L., Lin, Y., Han, J., Xi, Z., Shen, H., Gao, P., 2007. Magnetic resonance elastography of brain tumors: preliminary results. Acta Radiol. 48 (3), 327–330.
- Yin, Z., Hughes, J.D., Glaser, K.J., Manduca, A., Van Gompel, J., Link, M.J., Romano, A., Ehman, R.L., Huston III, J., 2017. Slip interface imaging based on MR-elastography preoperatively predicts meningioma-brain adhesion. J. Magn. Reson. Imaging 46 (4), 1007–1016.
- Yin, M., Venkatesh, S., Mariappan, Y., Glaser, K., Grimm, R., Manduca, A., Romano, A., Ehman, R., 2008. Value of shear wave attenuation as a tissue characterization parameter in MR elastography of the liver. In: Proc Intl Soc Mag Reson Med, Metro Toronto Convention Centre. p. 84.
- Zorgani, A., Souchon, R., Dinh, A.-H., Chapelon, J.-Y., Ménager, J.-M., Lounis, S., Rouvière, O., Catheline, S., 2015. Brain palpation from physiological vibrations using MRI. Proc. Natl. Acad. Sci. 112 (42), 12917–12921.